ELECTROMAGNETIC BACKSCATTERING BY PLATES AND DISKS

Semiannual Report

Constantine A. Balanis, Timothy Griesser, Diane M. Marsland
August 1, 1986-January 31, 1987

Department of Electrical and Computer Engineering
Arizona State University
Tempe, AZ 85287

Grant No. NAG-1-562
National Aeronautics and Space Administration
Langley Research Center
Hampton, VA 23665

ABSTRACT

With the recent development of diffraction coefficients for imperfectly conducting half-planes, it has become possible to analyze a wide variety of new problems for which the impedance surface boundary condition applies. This impedance boundary condition, while approximate, has been utilized to extend the usefulness of the Uniform Geometrical Theory of Diffraction (UTD) beyond the perfectly conducting geometries. In this report, these half-plane diffraction coefficients are used to analyze patterns of an antenna in the presence of an imperfectly conducting flat polygonal plate. This work supplements the well-known UTD problem of an antenna in the presence of a perfectly conducting ground plane, and it is extended to backscatter from flat plates and corner reflectors with surfaces which satisfy the impedance boundary conditions.

Geometrical Theory of Diffraction techniques were also used to investigate the backscattering from perfectly conducting plates. First the backscattering from a circular disk was analyzed using the GTD. First, second, and third order diffractions were included in the hard polarization analysis, while first, second, and second order slope diffractions were included in the soft polarization analysis. Improvements in the prediction of the monostatic radar cross section (RCS) over previous works were noted. For hard polarization an excellent agreement is exhibited between experimental and theoretical results, while a very good agreement is noted for soft polarization. To further improve the soft polarization results for wide angles, a model for the creeping wave or circulating current on the edge of the disk is obtained and used to find an additional component of the backscattered field. The addition of this component significantly improves the results for wide angles, leading to excellent agreement for soft polarization also. An axial-caustic correction method using equivalent currents is also included in the analysis.

The backscattering from a square plate is then analyzed using GTD. Backscattering in both the principal and off-principal planes is examined. For the principal plane case, the RCS is obtained using first, second and third order regular diffractions for hard polarization, and first order regular diffractions for soft polarization. For the off-principal plane case, the equivalent currents method is used with first and second order diffractions included for both polarizations. Very good agreement between the measured and predicted RCS is obtained for all angles and both polarizations for the principal plane case. Good agreement is also obtained for the off-principal plane case for both polarizations for small angles. However, due to possible cabibration problems of the measuring equipment, the results for larger angles are somewhat questionable.

I. SCATTERING BY LOSSY OR DIELECTRIC COVERED SURFACES

The Uniform Geometrical Theory of Diffraction [1] has been extended to be applicable to the imperfectly conducting half-plane [2]. The UTD coefficients of [2] remove the discontinuities in the total field at the incidence and reflection shadow boundaries. The coefficients are written in terms of the Maliuzhinets function of order π which has been approximated in terms of elementary functions [3]. The Maliuzhinets function arises from the solution of the boundary value problem of the canonical wedge with an impedance surface boundary condition. The validity of this boundary condition has been discussed in [4]. The edge is described by the relative surface impedance η and is considered to be opaque. The UTD coefficients of the imperfect conductor revert to the perfectly conducting UTD coefficients of [1] as η approaches zero for both normal and oblique incidences.

To analyze the pattern of an antenna in the presence of a polygonal plate, an extension of a method developed in [5] is utilized. In [5], an efficient and general technique is developed for analyzing the pattern of an arbitrary antenna in the presence of a polygonal plate using the UTD. The technique is readily developed into computer algorithms. With this technique, the most general problem can be analyzed by providing only the antenna orientation, pattern, frequency, and polarization and the polygonal plate shape, size and orientation. The total field pattern is a sum of the direct, reflected and singly diffracted fields. For the geometries considered, good agreement with experimental measurements was achieved in [5] without including higher

order diffractions. At the time [5] was published, corner diffraction theory was not completed and could not be included. This can lead to small discontinuities in the pattern if a diffraction point migrates off a finite edge. Since new corner diffraction coefficients for the imperfectly conducting finite edge are not available, these refinements cannot be included in this work either.

The described technique can be modified to imperfectly conducting surfaces of relative surface impedance η by adding the soft and hard reflection coefficients, Γ_s and Γ_h where $\Gamma_s=(\eta\sin\Psi-1)/(\eta\sin\Psi+1)$ and $\Gamma_h=(\sin\Psi-\eta)/(\sin\Psi+\eta)$ with the angle of incidence Ψ measured from the surface plane. The relative surface impedance η is defined as $\eta = Z_s/Z_0$ where Z_s is the surface impedance and Z_0 is the intrinsic impedance of free space [4]. These reflection coefficients are applicable only for good conductors or for high permittivity material as each assumes the propagation within the surface to be normal to the surface [4]. The diffraction coefficients D_s and D_h of the UTD are replaced by the 2×2 dyadic diffraction coefficient of [2]. This matrix of four nonzero dyads introduces cross polarization of the diffraction ray-fixed components. This ray-fixed field coupling is not present in the perfectly conducting case and hence must be incorporated into the formulation of [5].

The technique of determining the direct, reflected, and diffracted fields begins by rotating the source pattern to a global coordinate system according to the antenna orientation. The direct field, found by geometrical ray tracing, exists if the ray from the source in the

observation direction is not blocked by the plate. For the reflected field, a properly oriented image is positioned to guarantee equality of the angles of incidence and reflection. The image is at a point directly opposite the source through the plate. The reflected field exists if a ray from this image in the observation direction passes through the plate. The reflected field is a product of the incident field and the appropriate reflection coefficient Γ_s or Γ_h. The finite plate inherently causes discontinuities in the direct and reflected fields at the incidence and shadow boundaries associated with each edge of the plate. Diffracted fields must be added to remove these discontinuities. The diffraction point associated with each edge is found by constraining the diffraction direction to lie on the Keller cone. This diffraction point is best found iteratively using a search algorithm [5]. The diffraction exists only if a point satisfying the Keller cone requirement exists on the finite edge. Since the plate is polygonal, caustics will not be encountered. This is because at most one diffraction point can exist on each straight edge. However, the lack of a corner diffraction coefficient for imperfect conductors can lead to small discontinuities in the total field as the diffraction point drops off the finite edge.

Further improvement of the described method would be achieved by adding higher order diffractions. Second order diffractions, for example, would be included by locating points on two edges which satisfy the Keller cone requirement for a double diffracted ray optical field. For geometries in which the source or observation point lies near the plane of the flat plate, the spectral extensions of the UTD [6], which

account for the surface waves and higher order diffraction, will be required. The diffracted fields near edge-on incidence cannot be treated by ray optical techniques, and hence this spectral technique should be utilized. These corrections are of greatest importance in the forward scatter direction for doubly diffracted fields and in the backscatter direction for triply diffracted fields.

Preliminary computations for an antenna near a square plate, shown in Figure 1, have been performed. The plate is square measuring 10.596λ on a side and is centered in the y-z plane. The rectangular coordinates of the plate vertices are (0, ±5.298λ, ±5.298λ). Two examples of the pattern calculations are illustrated in Figures 2 and 3. These patterns represent the same cases considered in [5], and both cases provide good agreement with perfectly conducting ground plane measurements. The antenna is a short dipole oriented parallel to the z-axis, and the E_θ pattern in the azimuthal plane (θ=90°, 0°≤ϕ≤360°). is shown. The polar coordinate angle in Figures 2 and 3 represents the ϕ coordinate, and the patterns are normalized to a maximum of 0 dB. In Figure 2, the dipole is located at the rectangular coordinate (5.961λ, 0,0) and hence most of the direct field blockage is in the θ=90°, ϕ=180° direction. In Figure 3, the dipole is located at the rectangular coordinate (5.961λ, -4.857λ, 0) and hence the direct field blockage shifts toward θ=90°, ϕ=141°. The relative plate impedances considered are η = 0.001, 0.25, and 0.50. The η = 0.001 patterns are essentially identical to the perfectly conducting patterns. The effect of the lossy surface impedance is to reduce the strength of the reflected field and to alter the diffracted field. In

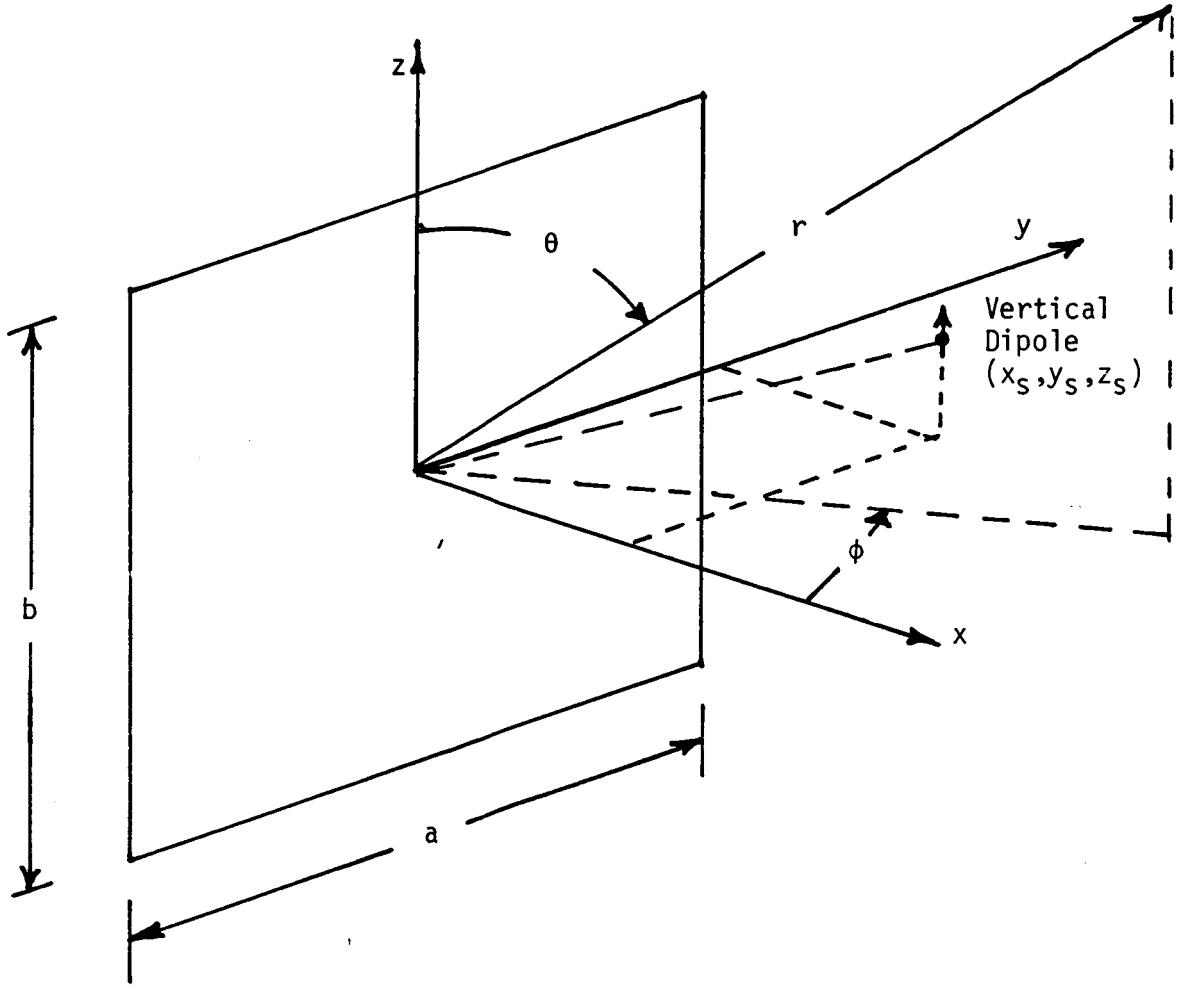

Figure 1. Vertical dipole in front of lossy plate.

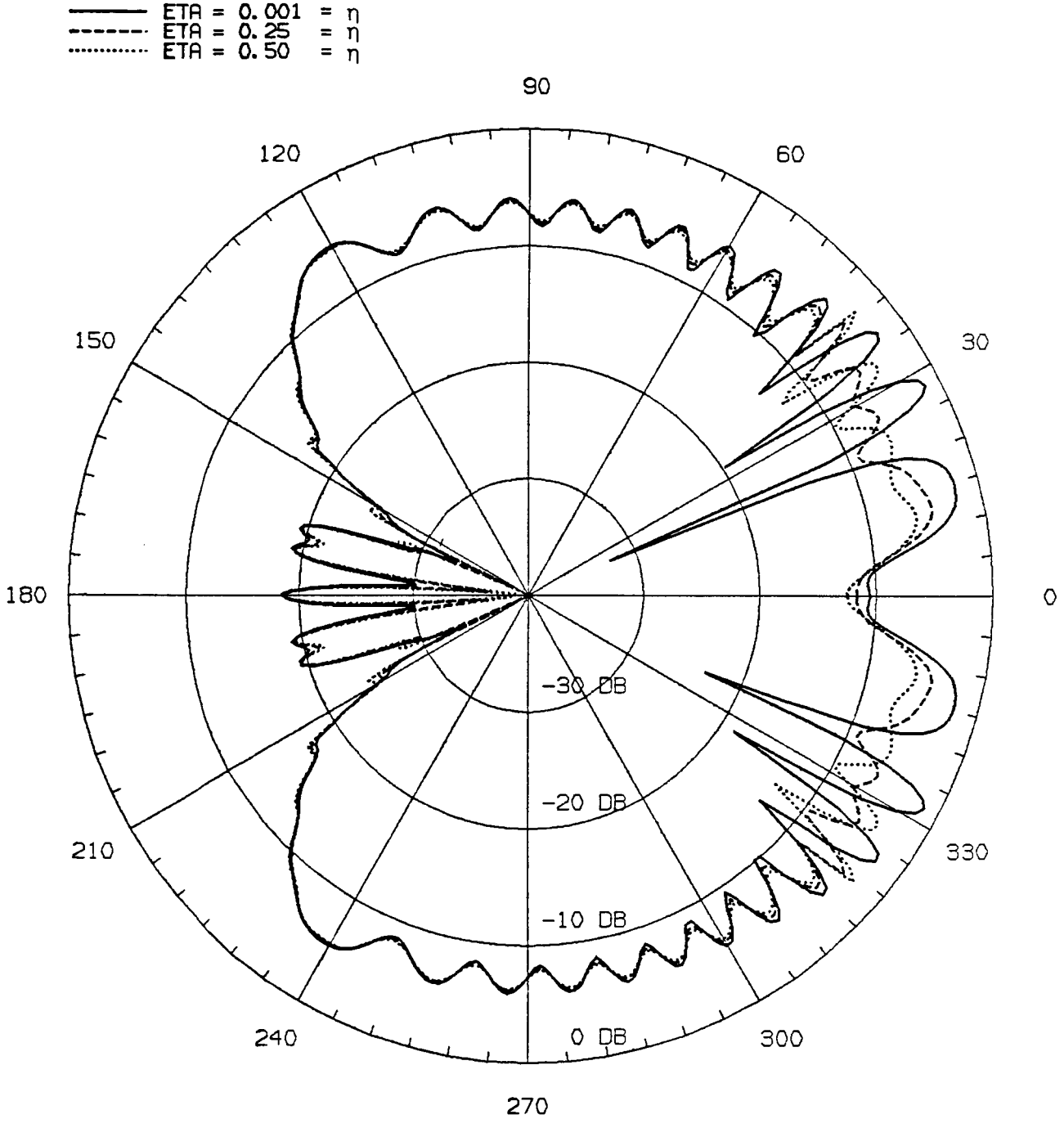

Figure 2. Azimuthal plane ($\theta = \pi/2$, $0 \leq \phi \leq 2\pi$) pattern of E_θ component of vertical dipole in front of lossy square plate ($a = b = 10.596\lambda$; $x_s = 5.961\lambda$, $y_s = z_s = 0$).

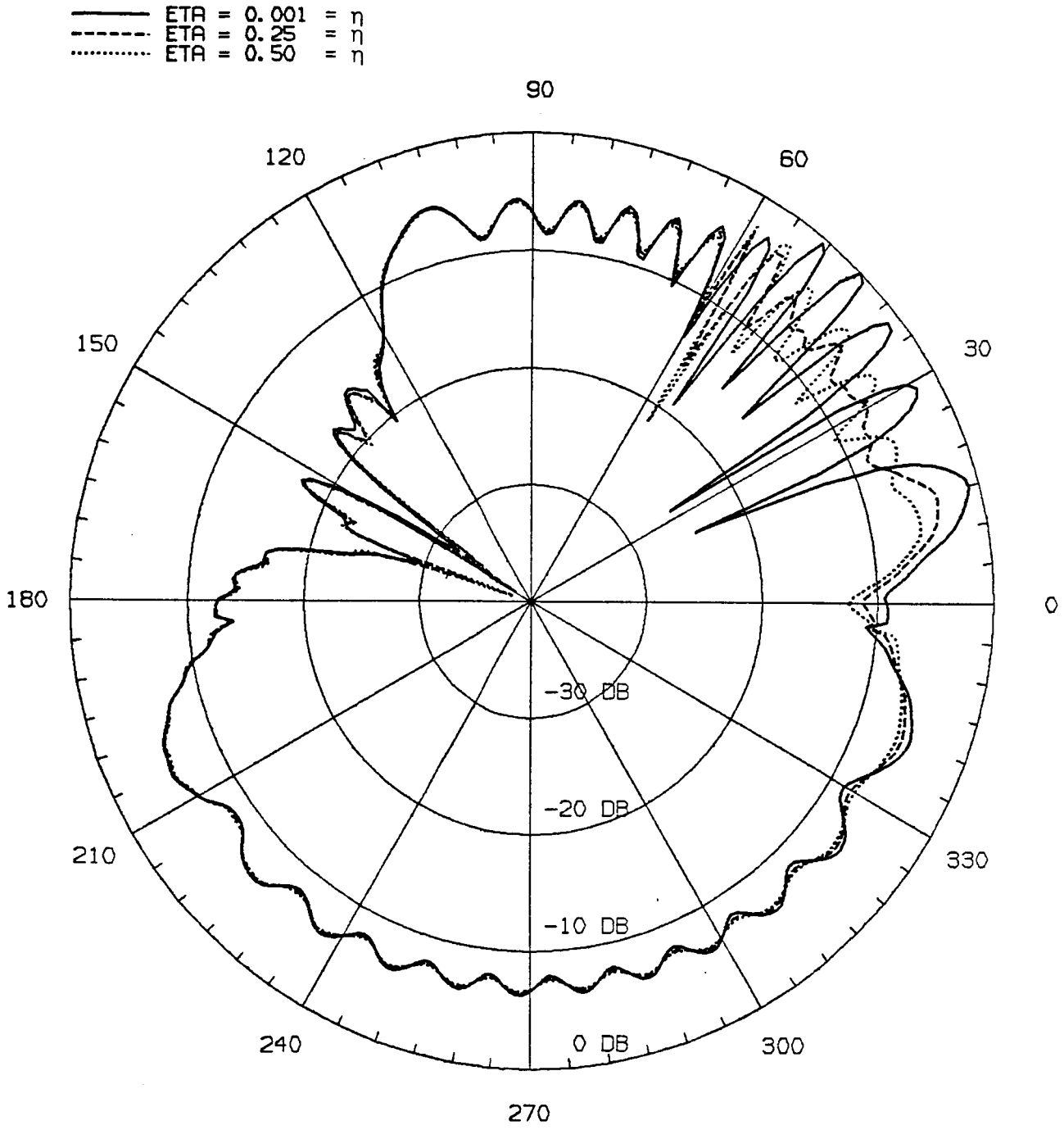

Figure 3. Azimuthal plane ($\theta = \pi/2$, $0 \leq \phi \leq 2\pi$) pattern of E_θ component of vertical dipole in front of lossy square plate ($a = b = 10.596\lambda$; $x_s = 5.961\lambda$, $y_s = -4.857\lambda$, $z_s = 0$).

the patterns, the large excursions of the peaks and nulls are reduced when the reflected field is no longer of the same strength as the direct field for lossy reflections.

The advantages of the recently developed UTD coefficient for the imperfectly conducting half-plane is evident by its usefulness in the general antenna/ground plane problem considered here. It is a straightforward extension of the UTD beyond the perfect conductor domain. Further work in the development of the UTD theory for arbitrary wedge angles and for corner diffractions will represent significant progress in this area.

These techniques are extended to backscattering problems, and they are presently under examination for such cases. It is expected that the amplitude scattering patterns of lossy surfaces will be less intense (compared to those from perfectly conducting surfaces). Therefore lossy surfaces are good candidates for applications whose objective is the reduction of the backscattering patterns.

II. BACKSCATTERING FROM A CIRCULAR DISK

In this section, the GTD is applied to the analysis of backscattering from a perfectly conducting circular disk. The disk is a very good example for showing the method in which GTD is applied to scattering problems since it involves the equivalent currents method, slope diffraction, curved edge diffraction, higher order diffraction and also a model for the creeping wave.

The objective of the analysis is to obtain an accurate and computationally efficient method for predicting the monostatic RCS of a circular disk. Many papers on this topic have been written in the past [7]-[11], and here it was desired to improve on these previous works further.

It is shown here that by using the UTD diffraction coefficients and by using first, second, and third order diffractions in the analysis for hard polarization, and first, second and slope diffractions in the soft polarization analysis yield excellent agreement between the theoretical and measured monostatic RCS patterns, especially for hard polarization.

For soft polarization, although significant improvements over previous works are obtained, a discrepancy is still noted at wide angles, and further improvement is desired. For this reason, a model for the creeping wave or circulating current on the edge of the disk is obtained and used to find an additional component of the backscattered field. This component adds the desired improvement to the RCS pattern, leading to excellent agreement between experiment and theory for soft polarization also.

This creeping wave, or circulating current, is induced on the edge of the disk for edge-on incidence. This wave will then shed energy tangentially at it travels around the circumference of the disk, as shown in Figure 4, thus contributing to the scattered field. Since most of the discrepancy is found at wide angles, it appears that incorporating this creeping wave effect into the analysis can add the desire improvement to the results.

The problem geometry is illustrated in Figure 5. The disk lies in the x-y plane. A plane wave in the y-z plane is incident at an angle θ to the z-axis. The RCS will be determined for values of θ from 0° to 90°. A time-dependence factor $e^{j\omega t}$ is assumed and suppressed throughout these calculations.

For soft polarization (electric field parallel to the plane of the disk) the incident E-field is:

$$\bar{E} = - \hat{a}_{\phi} E_o \, e^{\,jk(y\sin\theta+z\cos\theta)} = \hat{a}_x E_o e^{\,jk(y\sin\theta+z\cos\theta)} \qquad (1)$$

and for hard polarization (magnetic field parallel to the plane of the disk) the incident E-field is:

$$\bar{E} = - \hat{a}_{\theta} E_o e^{\,jk(y\sin\theta+z\cos\theta)} = (\hat{a}_y \cos\theta + \hat{a}_z \sin\theta) E_o e^{jk(y\sin\theta+z\cos\theta)} \qquad (2)$$

For angles removed from the axis ($\theta > 15^\circ$), point diffraction can be used. Because of axial caustics, equivalent current analysis is used for smaller angles ($\theta < 15^\circ$). The backscattered fields are obtained by determining the paths of all the reflected and diffracted rays that pass through the observation point, the spatial attenuation factor along these rays, the diffraction coefficient, the incident field at each

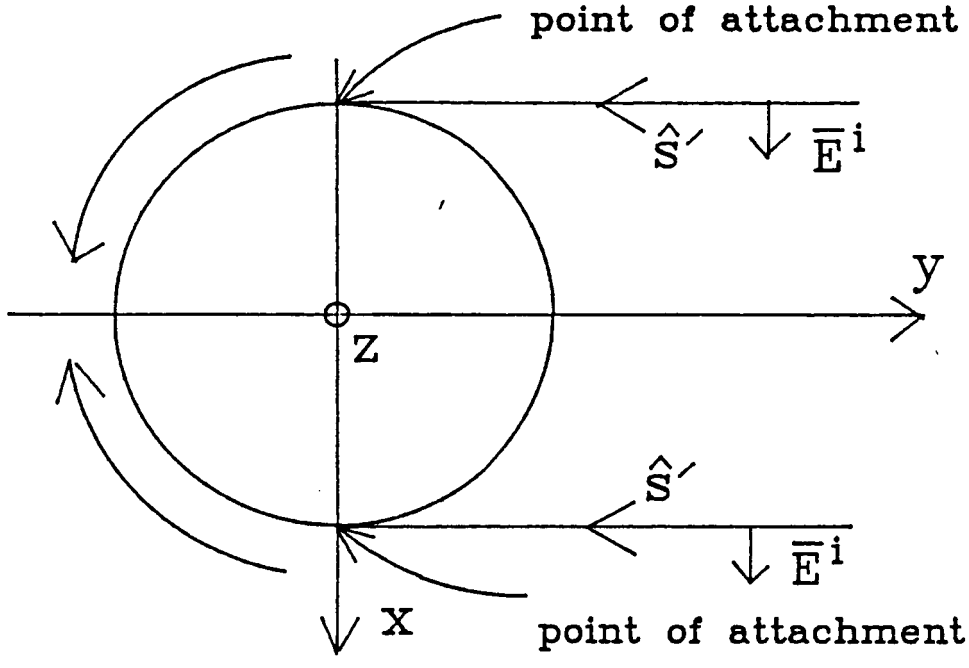

Figure 4. Illustration of creeping wave mechanism on a circular disk.

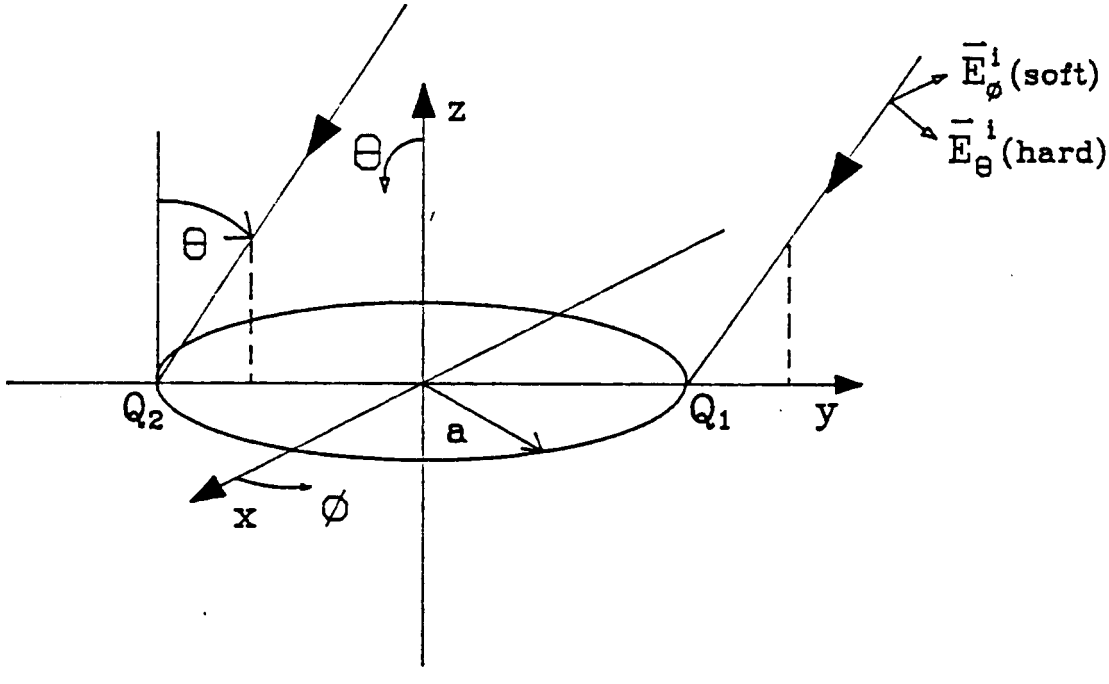

Figure 5. Geometry for backscattering from a circular disk.

point of diffraction, and a phase delay proportional to the distance from the edge. Thus, the mathematical form of the backscattered field is the product of these four factors which must be determined for each diffraction.

From geometry considerations alone, taking into consideration that the diffracted ray must lie on the Keller cone, it is found that first, second, and third order diffractions occur at points Q_1 and Q_2 (Figure 6). These points will be referred to as the "main" diffraction points. Second order diffractions are also possible at points Q_3 and Q_4, where $\beta = \beta'$. These points will be referred to as the "migrating" diffraction points since they depend on the angle of incidence. Even higher order diffractions can occur at the "main" diffraction points, and it may be possible to find additional points on the disk where higher order diffractions can occur. In this study, however, the diffractions mentioned above are the only ones considered, since for all the disks examined, it was found that any higher order diffractions, beyond third order, did not contribute significantly to the backscattered fields.

For the circular disk, computations and measurements of the monostatic RCS were made on 4" and 9" diameter disks at a frequency of 9.228 GHz. The thickness of the disks for the measurements was t=1/16". The RCS was obtained for both hard and soft polarization for each of the disks. The computations of the various orders of diffractions were compared with each other to determine the contribution of each, and the computations were compared with measurements to deterime the accuracy of the predictions. For soft polarization, the computed RCS patterns for diffractions only were also compared to the patterns with the additional

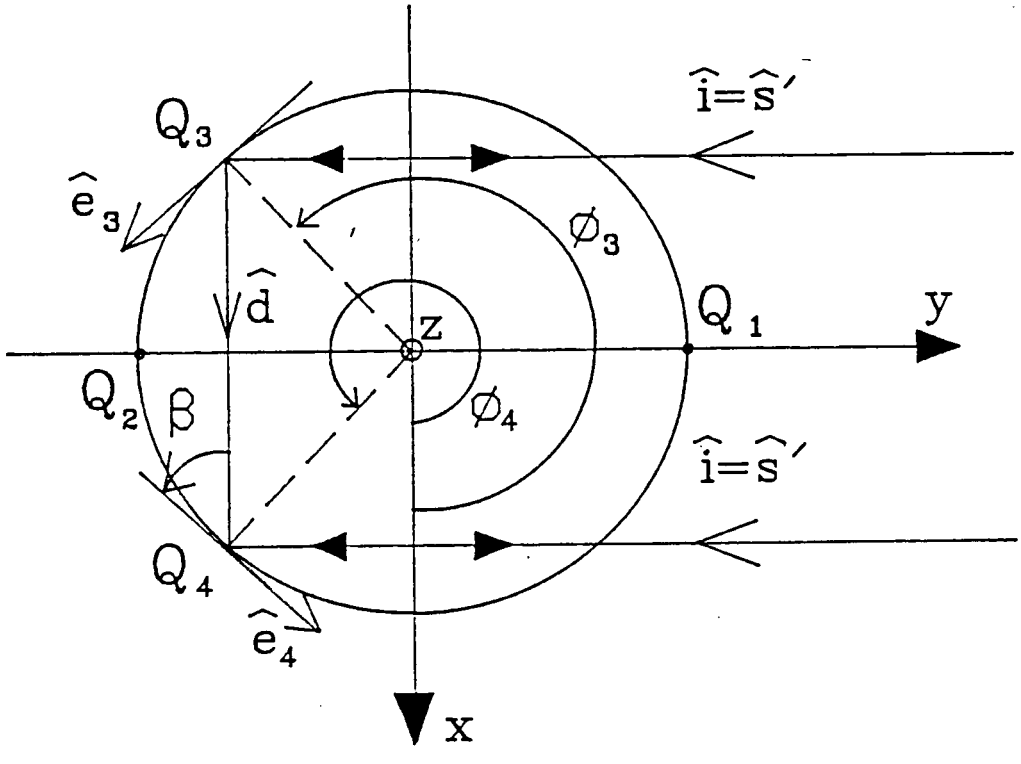

Figure 6. Diffraction points for backscattering from a circular disk.

creeping wave commponent, along with the measured patterns to see how the creeping wave component improves the predictions.

Figure 7 shows a comparison of the theoretical monostatic RCS patterns using first, first-second, and first-second-third order diffractions for hard polarization, for a 4" diameter disk. For the computations, an effective radius of 2.045" was used since it gave a more accurate prediction of the field. This is most likely necessary to compensate for the finite thickness of the disk [11] which the analytical model did not account for. The significant contribution of both the second and third order diffractions is evident, especially for the larger angles, and also around $\pm 45^{\circ}$ where the third order contribution adds a small lobe not present for the first and second order contributions.

Figure 8 shows a similar comparison of the theoretical monostatic RCS patterns for first, first-second, and first-second-third order diffractions for hard polarization, for a larger 9" diameter disk. In this case, an effective radius of 4.6035" was used for the same reason as was stated in the previous case. The significant contribution of both the second and third order diffractions is again evident, and the contribution of the third order diffractions is most pronounced for wide angles, near glancing incidence.

For the 4" diameter disk for soft polarization, Figure 9 illustrates the differences in the first, first-second, and first-second- slope diffractions for the RCS prediction. In this case, second order diffractions contribute very little to the RCS pattern, but the slope diffraction contribution has a significant effect on the pattern

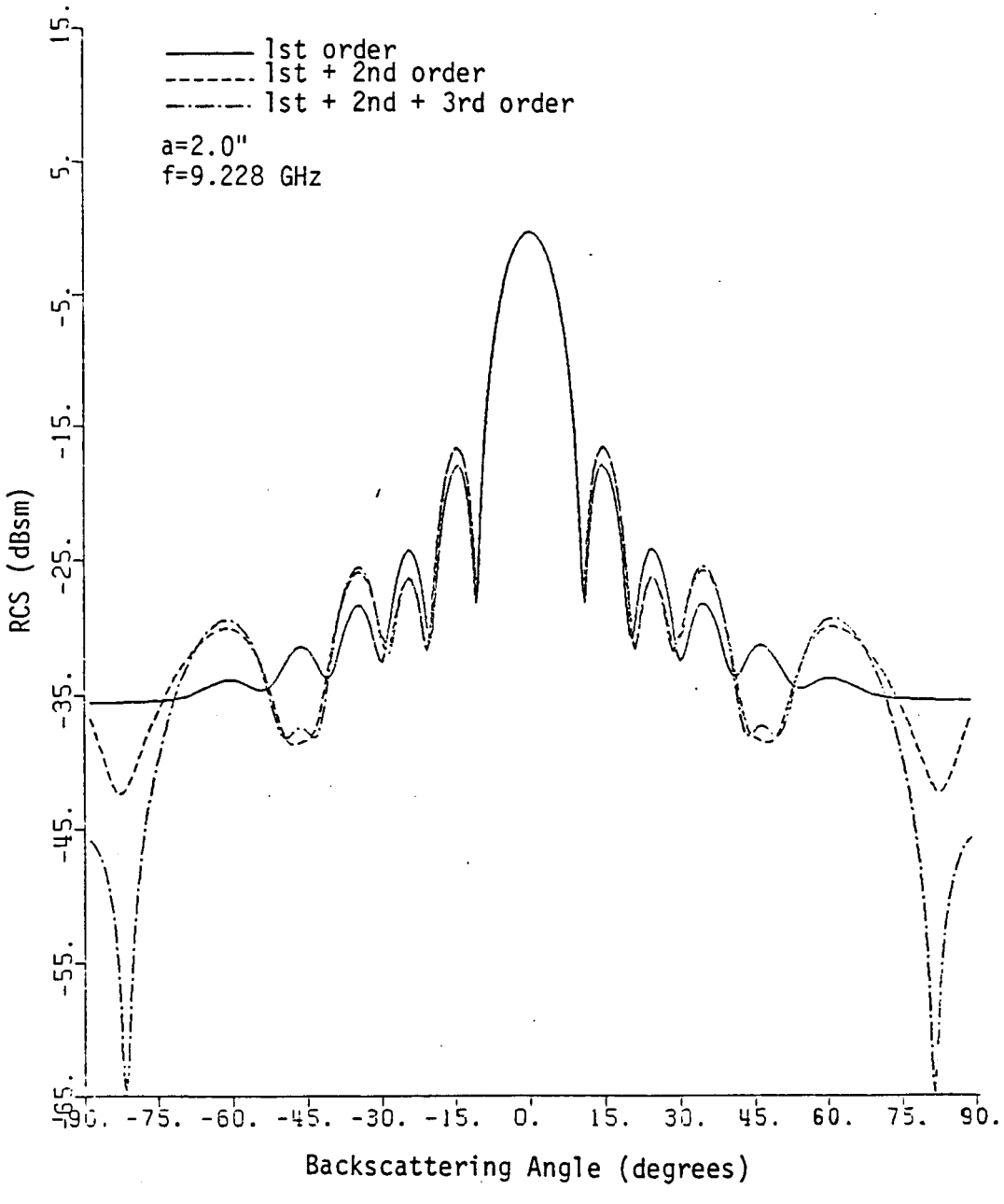

Figure 7. Hard polarization predicted monostatic RCS patterns of a circular disk.

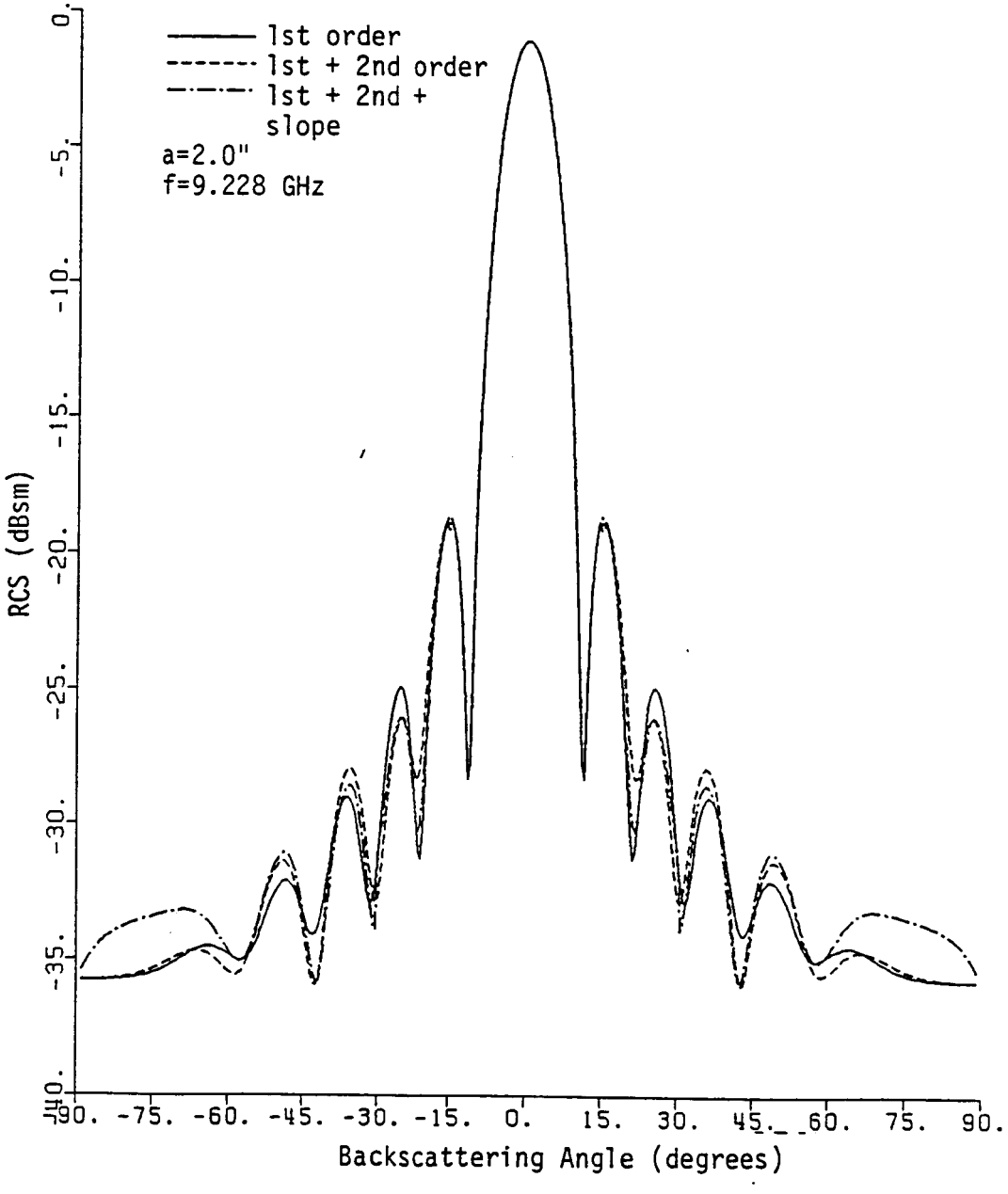

Figure 8. Soft polarization predicted monostatic RCS patterns of a circular disk.

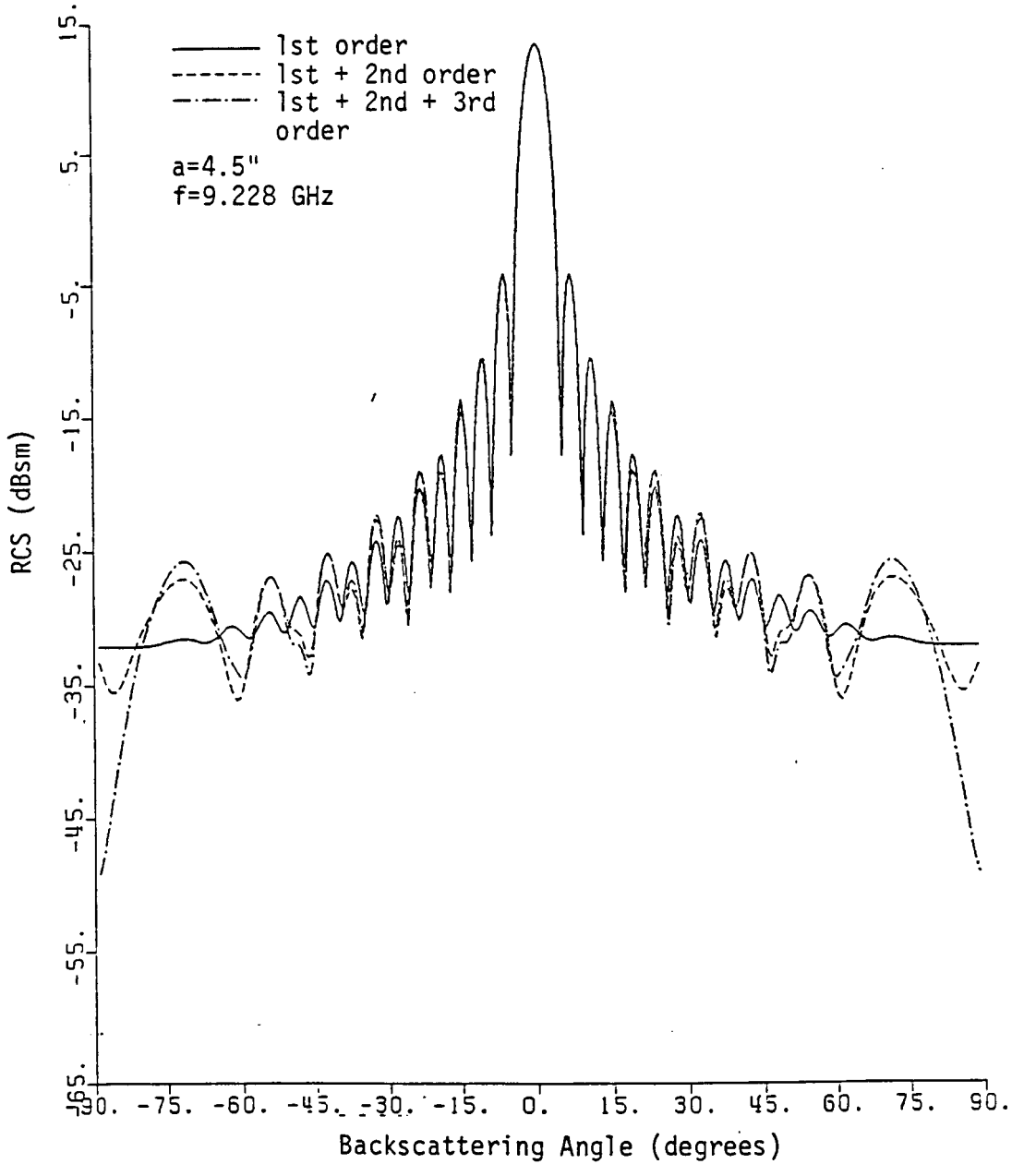

Figure 9. Hard polarization predicted monostatic RCS patterns of a circular disk.

for wide angles, $\theta>60^{\circ}$. As will be seen, the addition of the creeping wave component will also have a significant effect on the pattern for these wide angles.

For soft polarization for the larger 9" diameter disk, shown in Figure 10, there is even less of a difference between the different orders of diffraction. However, the slope diffraction contribution predicts a somewhat odd-shaped lobe around $\pm 60^{\circ}$, and it will be seen that this lobe, along with the creeping wave component matches the experimental data quite well.

Figure 11 shows a comparison of the computed and measured monostatic RCS patterns for the 4" diameter disk for hard polarization. The agreement is very good for all angles, and the theoretical computations even predict the small lobe around $\pm 45^{\circ}$. The RCS pattern comparisons for soft polarization for the smaller disk are seen in Figure 12. For this situation, both the computed patterns with and without the creeping wave component are included in order to better see the improvement due to the creeping wave. The improvement due to the addition of this creeping wave component is seen, and a very good agreement is obtained here also. In this case, the value of the propagation constant was varied slightly, to a value of $\nu=ka\{1-.65(-jka)^{-2/3}\}$, to better predict the pattern since, as mentioned earlier, the thickness of the plate can have a slight effect on this propagation constant.

The comparisons of the computed and measured monostatic RCS patterns for the larger 9" diameter disk for hard polarization are seen

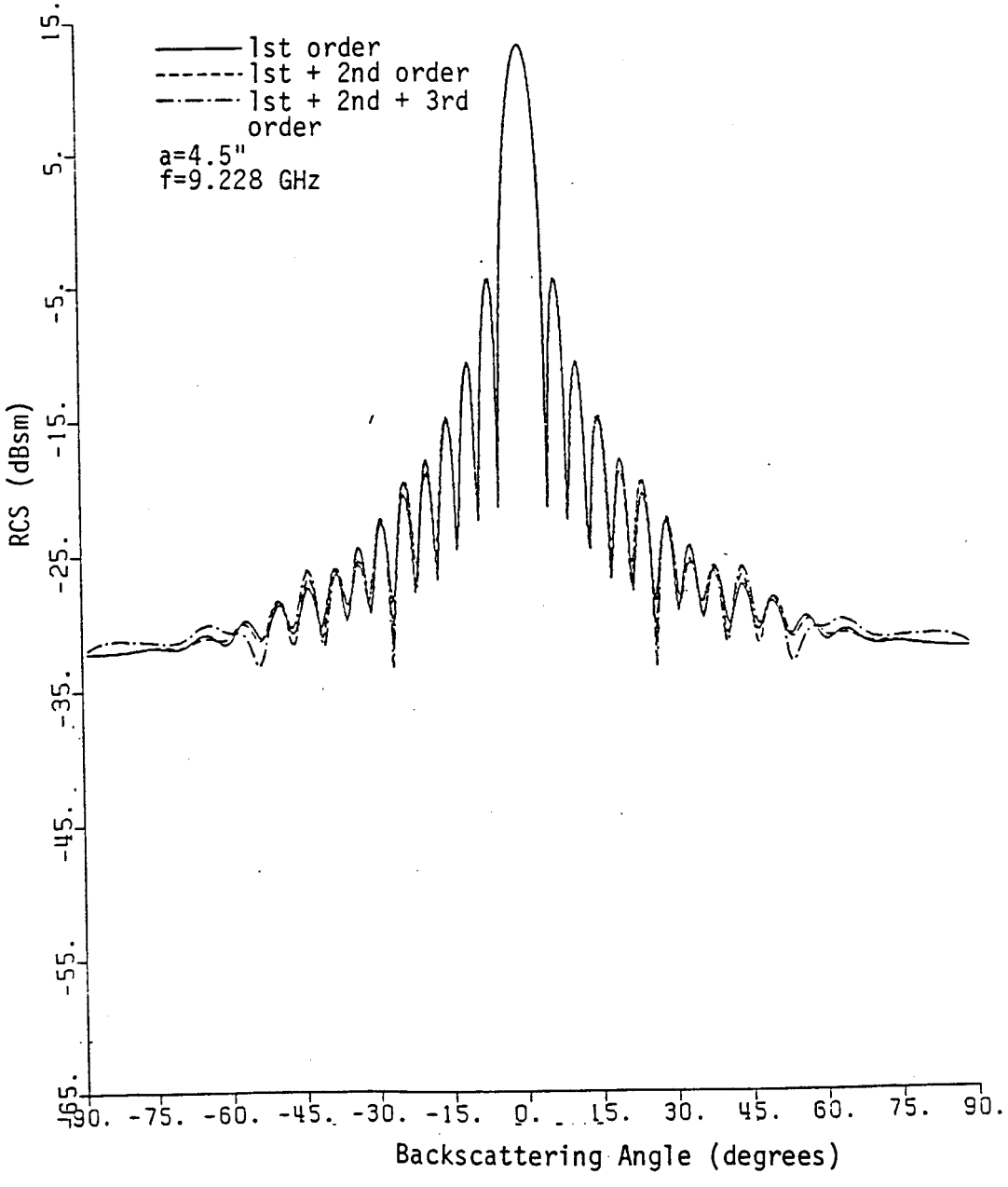

Figure 10. Soft polarization predicted monostatic RCS patterns of a circular disk.

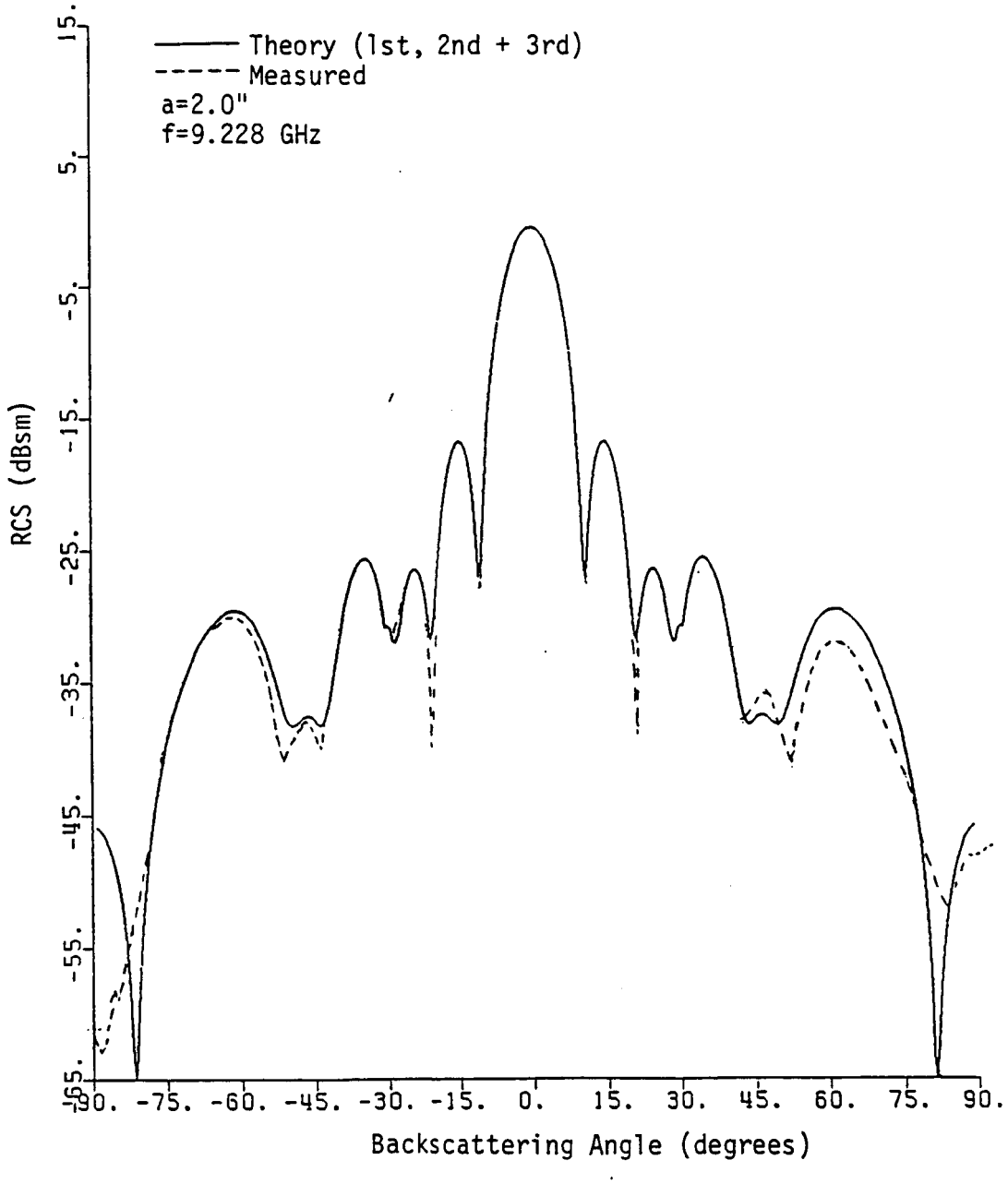

Figure 11. Hard polarization measured and predicted monostatic RCS patterns of a circular disk.

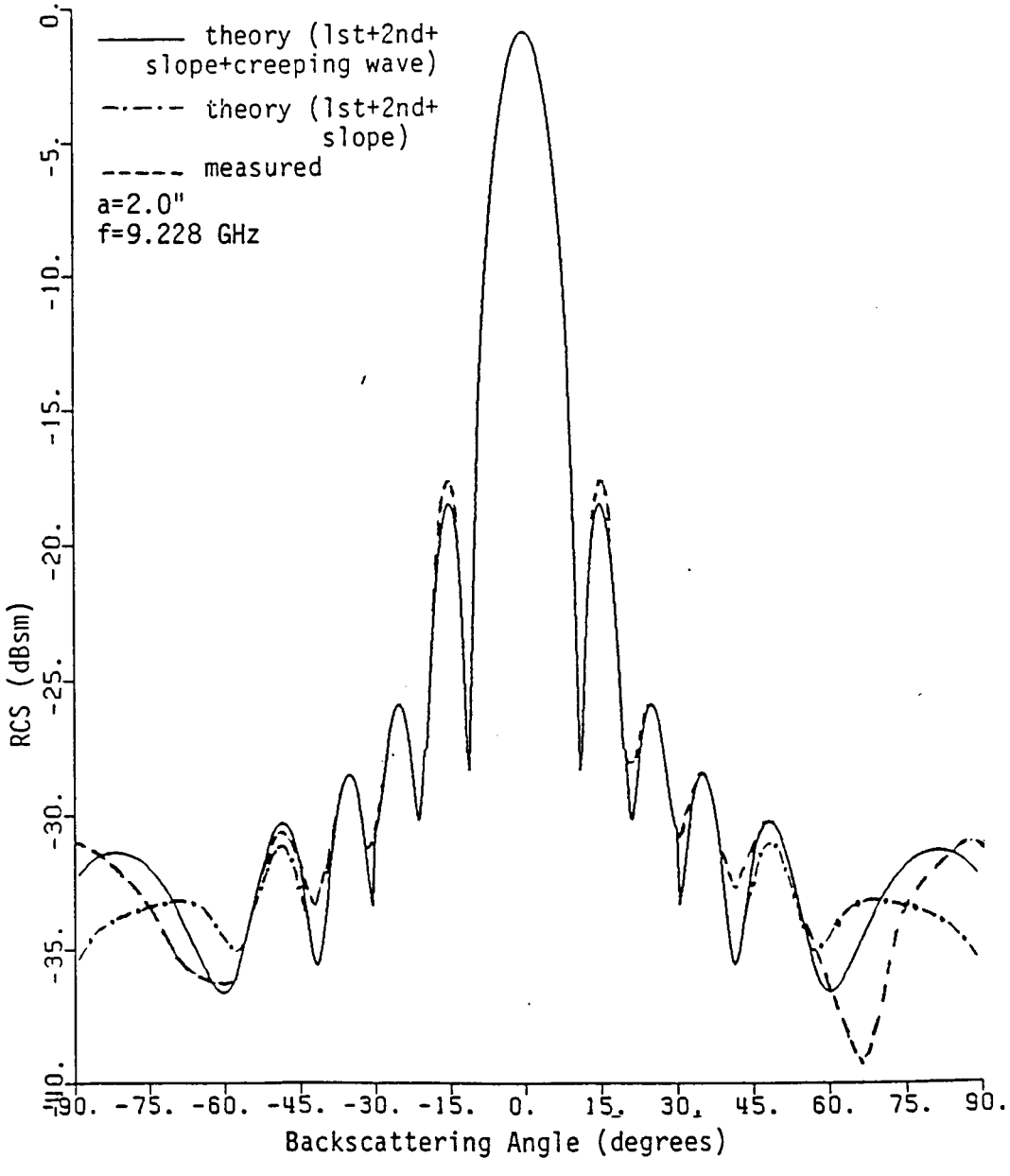

Figure 12. Soft polarization measured and predicted monostatic RCS patterns of a circular disk.

in Figure 13. As can be seen, the agreement between the theoretical and experimental patterns is excellent, and the theory predicts some of the finer detail of the structure very well. Figure 14 shows a similar comparison for soft polarization. Again, both the computed patterns with and without the creeping wave component are included in order to better see the improvement due to the creeping wave. Notice that the odd-shaped lobe, predicted by the additional slope diffraction component, is present in the experimental data. Also, the addition of the creeping wave component has a significant effect on the pattern for the wide angles, and the agreement between theory and experiment is greatly improved by this additional component. In fact, the agreement between the experimental and theoretical patterns is excellent, and the theory predicts the structure very well.

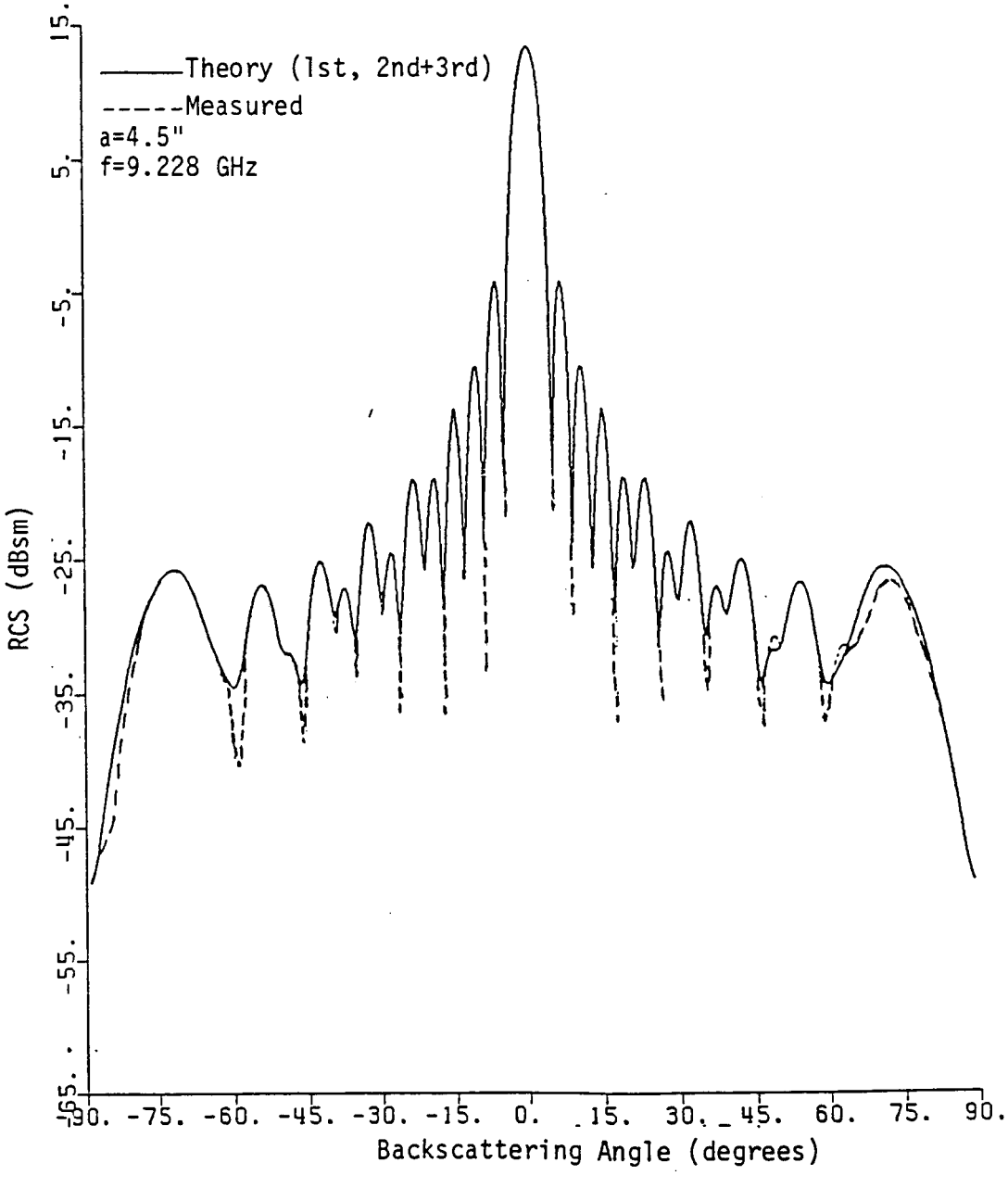

Figure 13. Hard polarization measured and predicted monostatic RCS patterns of a circular disk.

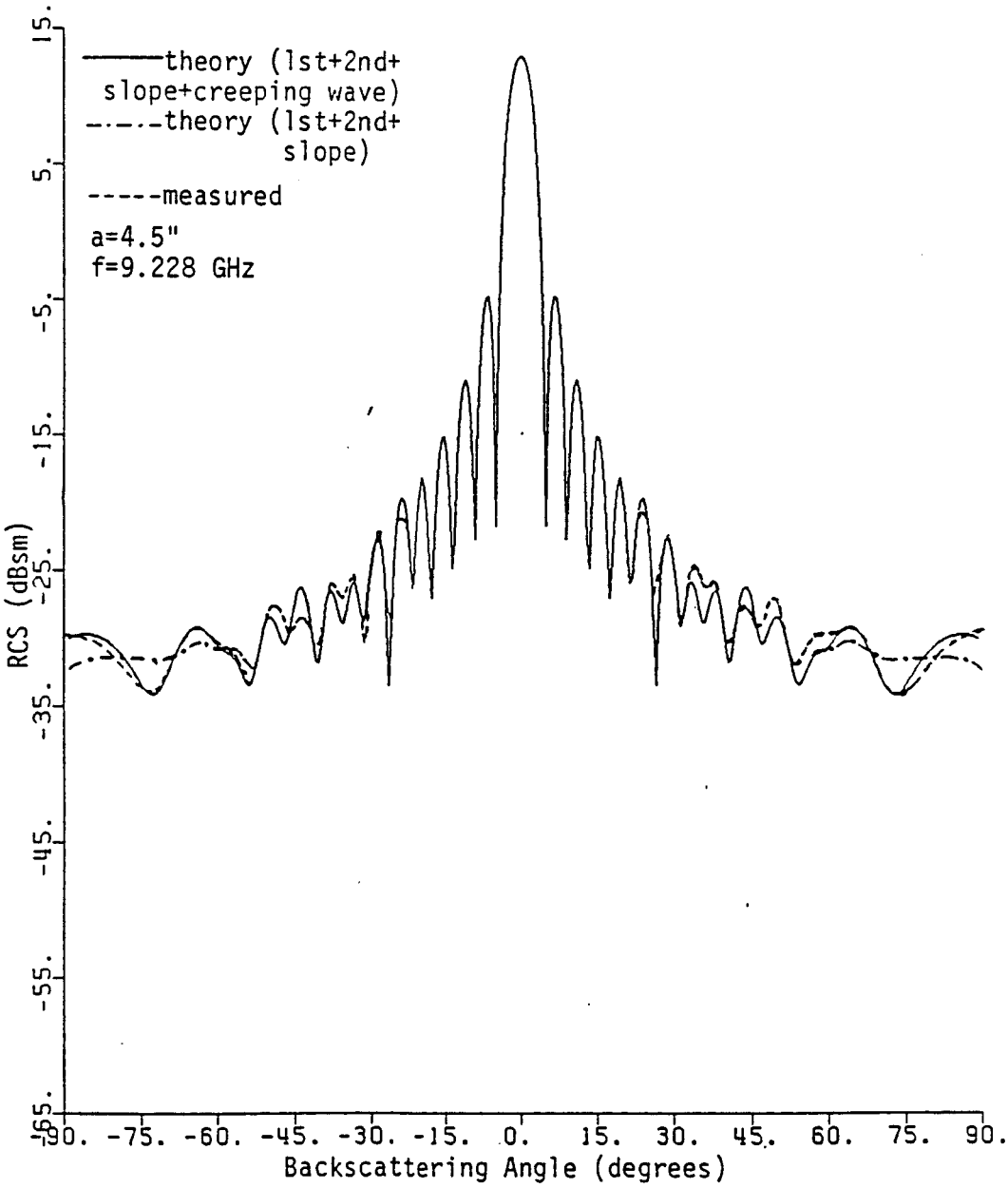

Figure 14. Soft polarization measured and predicted monostatic RCS patterns of a circular disk.

III. BACKSCATTERING FROM A SQUARE PLATE

In this section, the GTD is applied to the analysis of backscattering from a perfectly conducting square plate. In order to find the backscattered fields, principal plane and off-principal plane backscattering are considered seperately. Principal plane backscattering refers to the case where the incident and scattered fields lie in a plane perpendicular to two edges of the plate. Off-principal plane backscattering is the term used for all other situations. The principal plane problem has been addressed by many authors in the past. However, studies on off-principal plane backscattering are more difficulty, and more accurate and efficient ways of handling the problem are desired. The off-principal plane case is of particular importance because of its generality since it can give insight into the mechanisms involved in the scattering from a target randomly oriented in space. Methods for handling both principal and off-principal plane backscattering are presented here with higher order diffractions incorporated into the analysis.

Referring to Figure 15, scattering in the planes $0 \leqq \phi \leqq 45^\circ$ need only be considered due to the symmetry of the problem. This corresponds to a plate tilt of 0° to 45°. A plate tilt φ greater than 45° is the same as a tilt of $90^\circ - \varphi$ due to symmetry.

For principal plane backscattering ($\phi = 0^\circ$), the diffracted rays do lie on the Keller cone and GTD (UTD) point diffraction can be used. This allows for easy inclusion of higher order diffractions. The

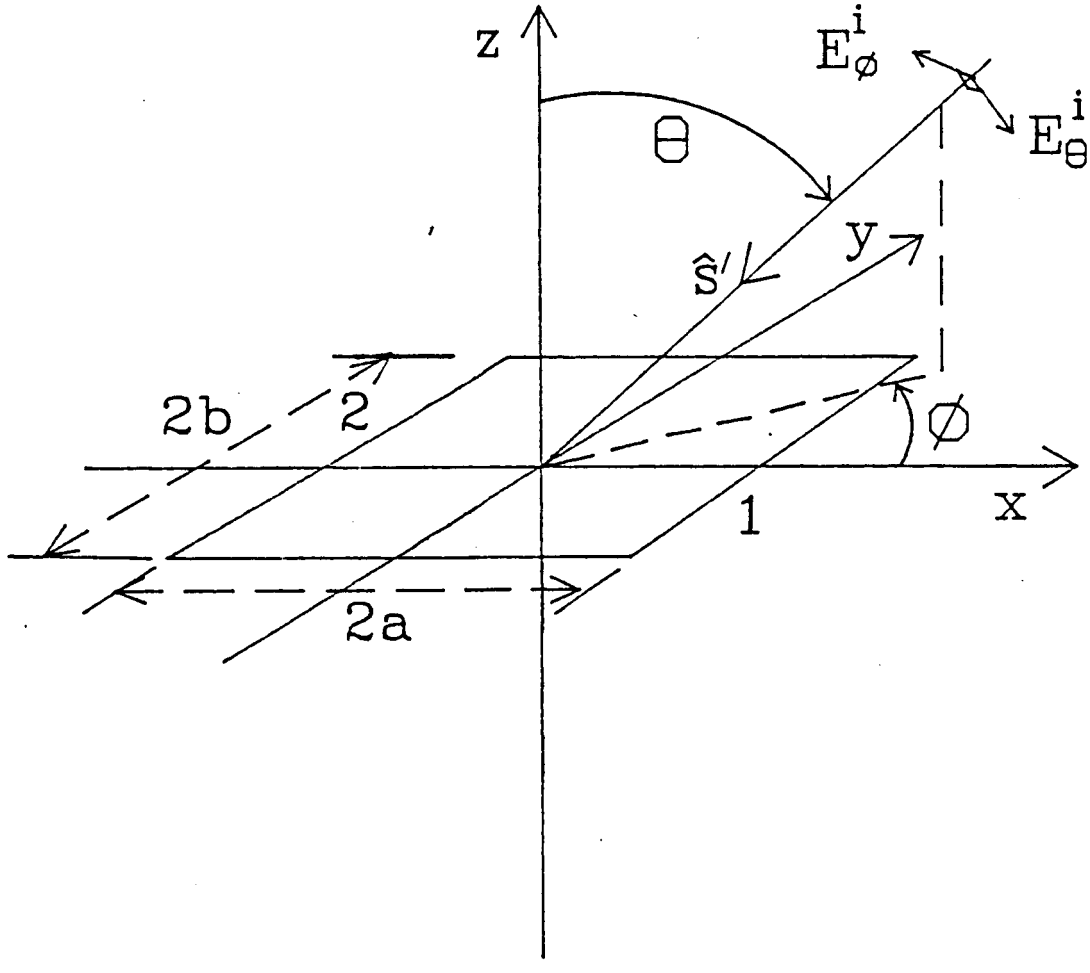

Figure 15. Geometry for backscattering from a square plate.

diffracted fields, first and higher orders, are obtained using two-point diffraction from a strip. Then using the relation between the two-dimensional and three-dimensional fields of

$$E_{3\text{-}d} = \frac{\ell e^{j\pi/4}}{\sqrt{\lambda r}} E_{2\text{-}d} \qquad (3)$$

the RCS of the square plate is obtained. For hard polarization, first, second, and third order diffractions are considered. The higher order diffracted fields are only obtained for hard polarization since for soft polarization, the diffracted ray traveling between the two diffraction points has its E-field in the plane of the plate, and therefore must be zero. In this case, a slope diffraction could be used [12]. However, for the square plate for soft polarization, first order diffractions alone are sufficient for an accurate prediction of the monostatic RCS.

For off-principal plane backscattering, the diffracted rays will not lie on the Keller cone and therefore, the equivalent currents method must be used. The first order diffracted field is obtained by placing the Michaeli equivalent currents of [13] on edges 1 and 2. Both electric and magnetic equivalent currents are used since there are components of both the E and H field parallel to edges 1 and 2. The backscattered fields are then obtained from the far-field radiation integrals.

Second order diffractions are included in this analysis by considering the manner in which the diffracted fields from a first order point diffraction will illuminate the opposite edge. The second order equivalent current is then obtained at the second edge and is integrated over the illuminated portion to find the second order backscattered

field.

The principal plane backscattered field can also be obtained using the above method since it is just a special case, $\phi=0^{\circ}$. However, the results obtained using point diffraction will be more accurate since even higher order diffractions are included in the analysis.

III-1. Principal Plane Backscattering

The problem geometry for principal plane backscattering from a square plate is shown in Figure 16. Principal plane backscattering is just a special case of off-principal plane backscattering where $\phi=0^{\circ}$. Therefore, the results from the off-principal plane backscattering could be used to obtain the scattered fields here. However, since the diffracted rays lie on the Keller cone, a much more accurate prediction can be obtained by using GTD point diffraction, because higher order diffractions can be easily incorporated into the analysis.

III-2. Off-Principal Plane Backscattering

The diffracted fields for off-principal plane backscattering do not lie on the Keller cone, and therefore the Michaeli equivalent currents of [13] must be used for first order diffractions. However, if these currents are used for the second order diffractions, they would become infinite at glancing incidence. Therefore, the new Michaeli currents [14], [15] must be used for second order diffractions.

For this situation, the incident E-field will be assumed to be

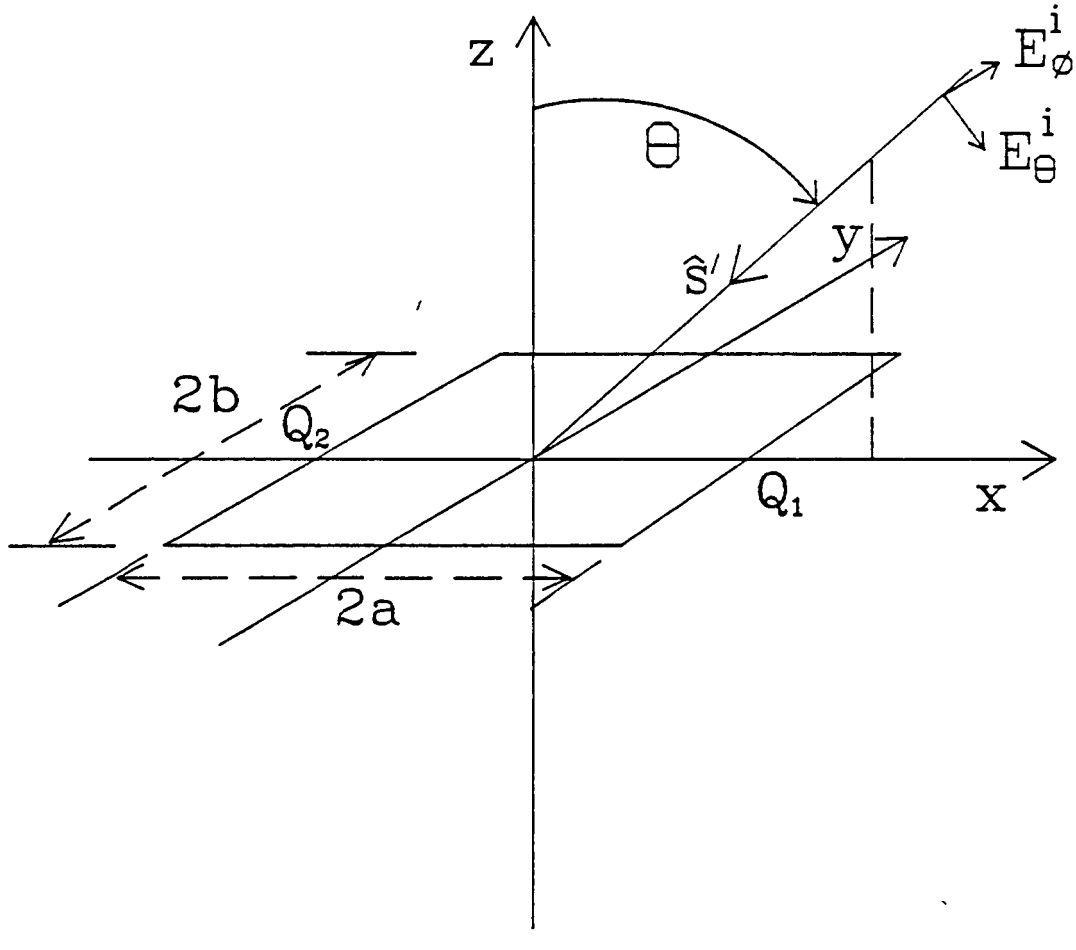

Figure 16. Backscattering in a principal plane of a square plate.

polarized in either the $\hat{\theta}$ or $\hat{\phi}$ direction as for the disk, and can be written as

$$E_\theta^i = -\hat{a}_\theta e^{jk(x\sin\theta\cos\phi+y\sin\theta\sin\phi+z\cos\theta)}$$

$$= [-\hat{a}_x\cos\theta\cos\phi-\hat{a}_y\cos\theta\sin\phi+\hat{a}_z\sin\theta]\ e^{jk(x\sin\theta\cos\phi+y\sin\theta\sin\phi+z\cos\theta)} \quad (4)$$

$$E_\phi^i = -\hat{a}_\phi e^{jk(x\sin\theta\cos\phi+y\sin\theta\sin\phi+z\cos\theta)}$$

$$= [\hat{a}_x\sin\phi-\hat{a}_y\cos\phi]e^{jk(x\sin\theta\cos\phi+y\sin\theta\sin\phi+z\cos\theta)} \quad (5)$$

Likewise, the corresponding incident magnetic fields can be written as

$$H_\phi^i = \hat{a}_\phi e^{jk(x\sin\theta\cos\phi+y\sin\theta\sin\phi+z\cos\theta)}$$

$$= [-\hat{a}_x\sin\phi+\hat{a}_y\cos\phi]\ e^{jk(x\sin\theta\cos\phi+y\sin\theta\sin\phi+z\cos\theta)} \quad (6)$$

$$H_\theta^i = -\hat{a}_\theta e^{jk(x\sin\theta\cos\phi+y\sin\theta\sin\phi+z\cos\theta)}$$

$$= [-\hat{a}_x\cos\theta\cos\phi-\hat{a}_y\cos\theta\sin\phi+\hat{a}_z\sin\theta]e^{jk(x\sin\theta\cos\phi+y\sin\theta\sin\phi+z\cos\theta)} \quad (7)$$

However, for this case, $\hat{\theta}$ ($\hat{\phi}$) does not correspond to an incident field of strictly hard (soft) polarization since there will be components of the incident field both parallel and perpendicular to the plane of incidence. The incident fields could be referred to as vertically (E_ϕ^i) or horizontally (E_θ^i) polarized if the plate is assumed to be oriented vertically in space, and rotating around a vertical axis.

III-3. Computations and Comparisons with Measurements

Computations and measurements of the monostatic RCS were made on a

6.747"×6.747" square plate at a frequency of 10 GHz for both vertical (E_ϕ incident) and horizontal (E_θ incident) polarization. The primary polarization RCS was computed and measured only. Therefore, the vertical polarization case can be referred to as VV (vertical incident polarization, vertical scattered polarization), and the horizontal case can likewise be referred to as HH. Computations and measurements were made for the principal plane case ($\phi=0^\circ$), and for off-principal plane cases for $\phi=30^\circ$ and $\phi=45^\circ$. The measurements for the square plate are slightly inaccurate ($\simeq$ 2 dBsm too low) at the peak of the major lobe at normal incidence due to possible calibration problems in the measuring equipment. The actual value of the RCS of a flat plate at normal incidence is well known and is predicted extremely well by PO and by GTD. Therefore, the difference found here between the measurements and theory at normal incidence is not an inaccuracy of the theory, but rather an experimental inaccuracy and will not be discussed further in the following comparisons which address the accuracy of the theoretical predictions.

Figure 17 shows the comparison of the measured and theoretical monostatic RCS for the principal plane case for VV (soft) polarization. In this case, only first order diffractions were included in the analysis, and as can be seen, very good agreement was still obtained. The theory predicted the RCS quite well for most angles. Some ambiguity due to the sensitivity limitations of the measuring equipment at low signal levels is evident for large angles $\theta>70^\circ$. However, the theoretical pattern still seems to predict the behavior fairly well.

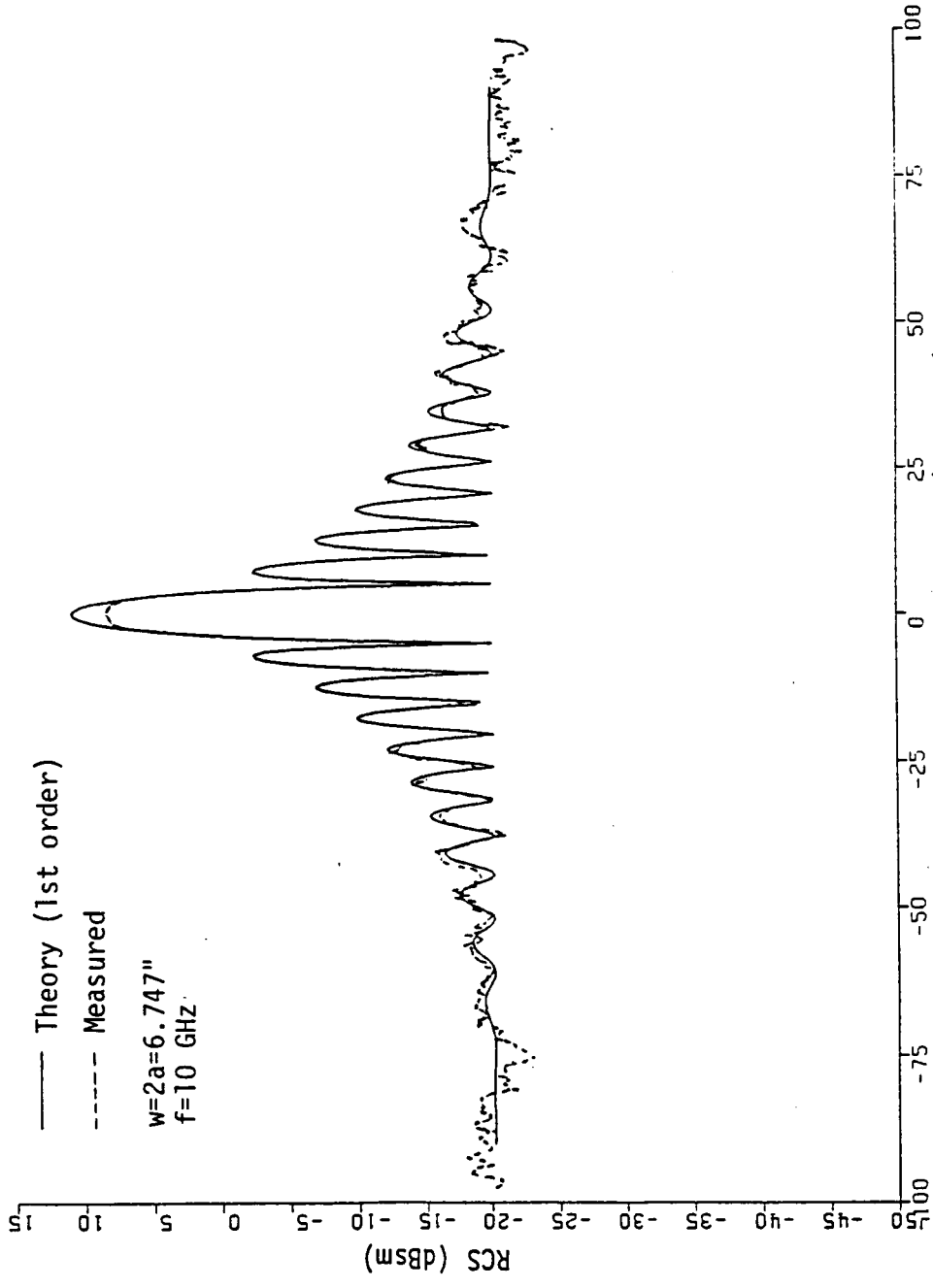

Figure 17. VV (soft) polarization measured and predicted monostatic RCS patterns of a square plate in the principal plane.

A similar comparison for HH (hard) polarization is shown in Figure 18. In this case, the agreement is very good for all angles and the theoretical prediction, which includes up to third order diffractions, predicts the RCS quite well.

For the off-principal plane cases, the comparison is somewhat more difficult because of ambiguities present in the measurements. The patterns should be symmetric about $\theta=0^{\circ}$, but they are not due to possible errors in the measuring system. The symmetry problem occurs because of the great difficulty in positioning the target at this off-principal plane angle. However, comparisons can still be made, especially for the smaller angles, and a general idea of overall accuracy of the theoretical predictions can still be obtained.

For $\phi=30^{\circ}$, Figure 19 shows a comparison of the theoretical versus experimental RCS patterns for VV polarization. The agreement is good for small angles near normal incidence, and for larger angles, the same type of behavior in the two patterns can be seen, such as the position of the lobes, although the actual magnitudes are quite different. Second order diffractions were included in the theoretical patterns; however, the difference between first and first-second order diffractions was very small as can be seen in the figure. For the HH polarization case, shown in Figure 20, again the agreement is good for small angles, but the theoretical pattern deviates from the measured pattern for the larger angles. Again, the measurements are somewhat questionable for these larger angles since they are not symmetric and because of the possible calibration problems in the measuring equipment. However, the prediction does seem to show the same type of behavior, and

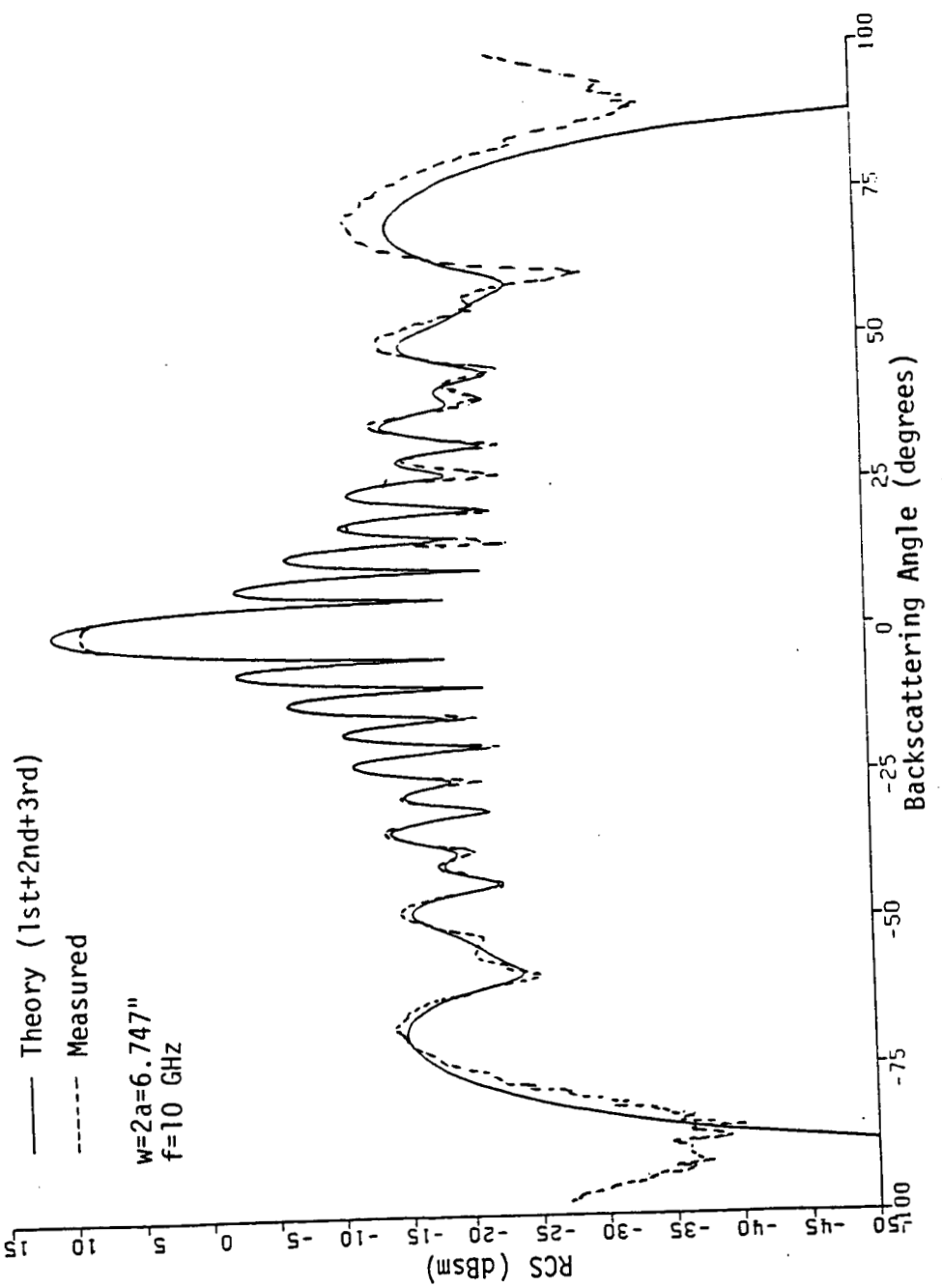

Figure 18. HH (hard) polarization measured and predicted monostatic RCS patterns of a square plate in the principal plane.

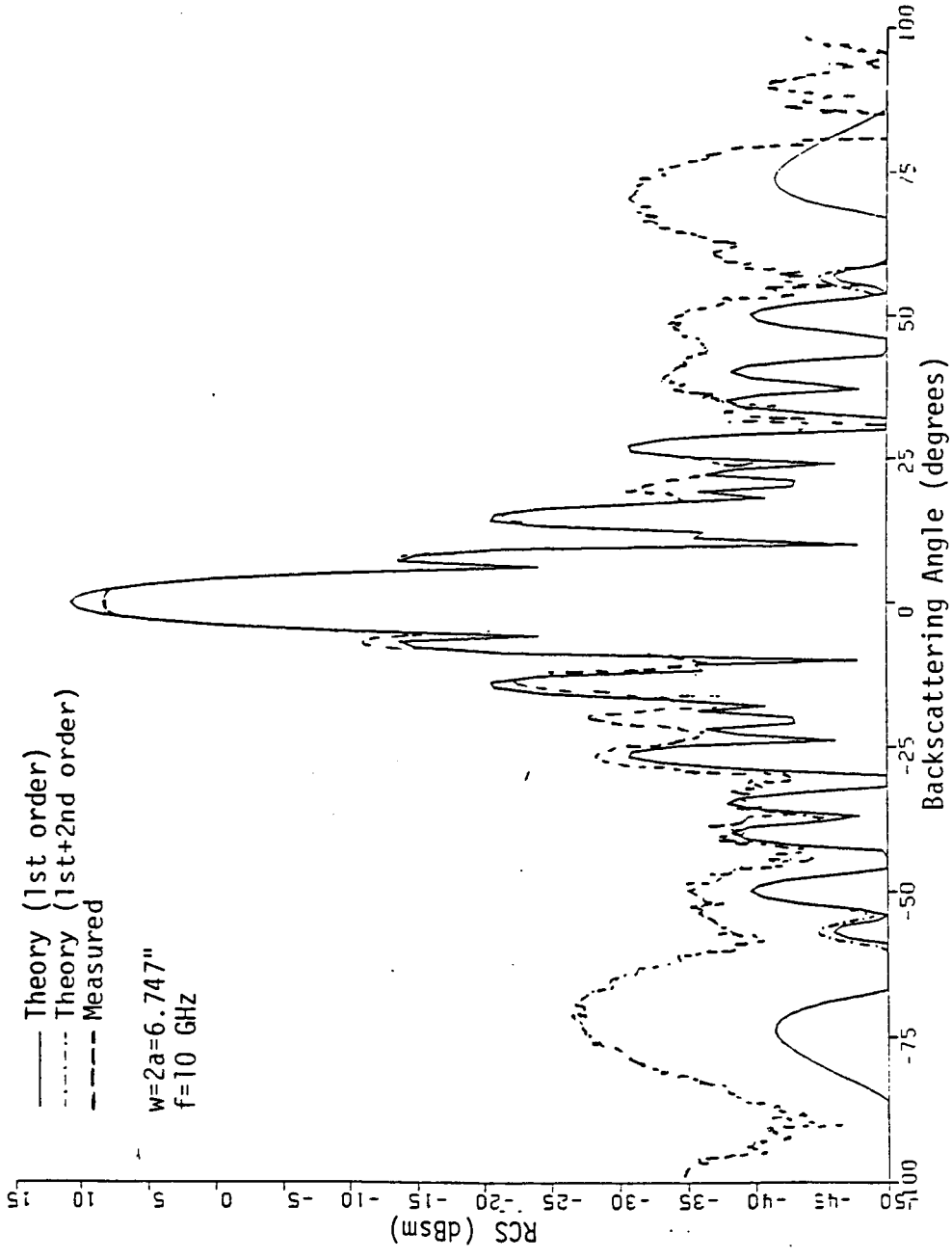

Figure 19. Primary VV polarization measured and predicted monostatic RCS patterns of a square plate in the off-principal plane $\phi = 30°$.

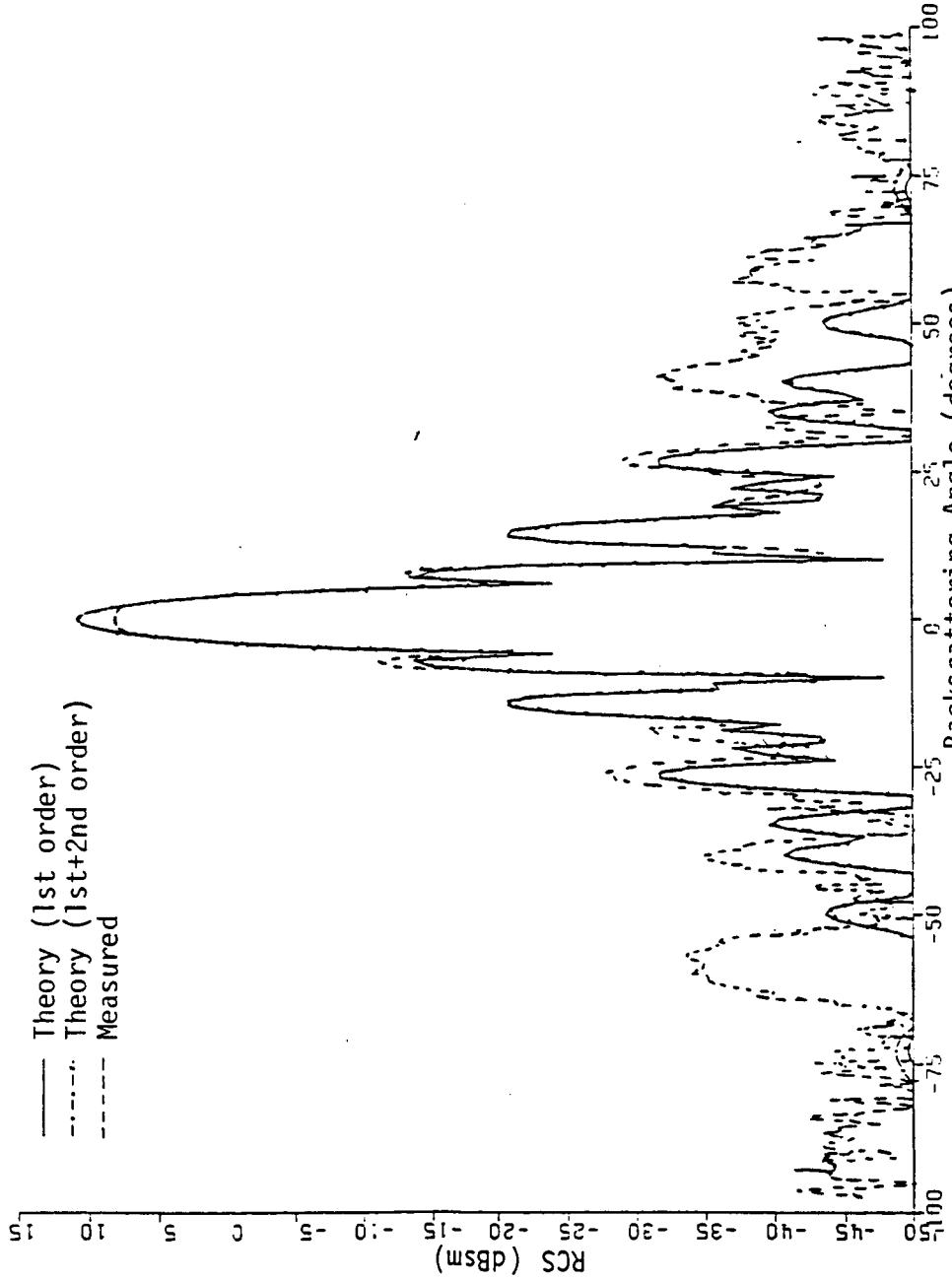

Figure 20. Primary HH polarization measured and predicted monostatic RCS patterns of a square plate in the off-principal plane $\phi = 30°$.

as can be seen in the figure, becomes quite small for large angles, as does the experimental pattern. In this case, again the difference between first and first-second order diffractions was insignificant, making only a slight difference in the size of the small lobe around $\pm 75^{\circ}$.

Figure 21 shows the comparison for $\phi=45^{\circ}$ for VV polarization. As for the 30° case, the agreement is good for small angles, but not for the larger angles. However, the placement of the lobes seems to be predicted fairly well by the theoretical pattern, and due to the ambiguity of the measurements, the degree of accuracy is difficult to determine. The large lobe at $\pm 75^{\circ}$ is evident in the measured data, and occurs symmetrically about $\theta=0^{\circ}$, and the theory does not predict the magnitude of this lobe very well. However, for this specific case, some mechanism should probably be included in the analysis to handle the corner correctly. This has not been included in this analysis. For HH polarization for the same case (Figure 22), the agreement seems to be a somewhat better since only the lobes near normal incidence are significant, and for larger angles, the measured data appears to be predominantly noise. This type of behavior is predicted well by the theory since for $\theta>50^{\circ}$ the RCS is insignificant. Second order diffractions are not included for the special case $\phi=45^{\circ}$ because the opposite side is not illuminated.

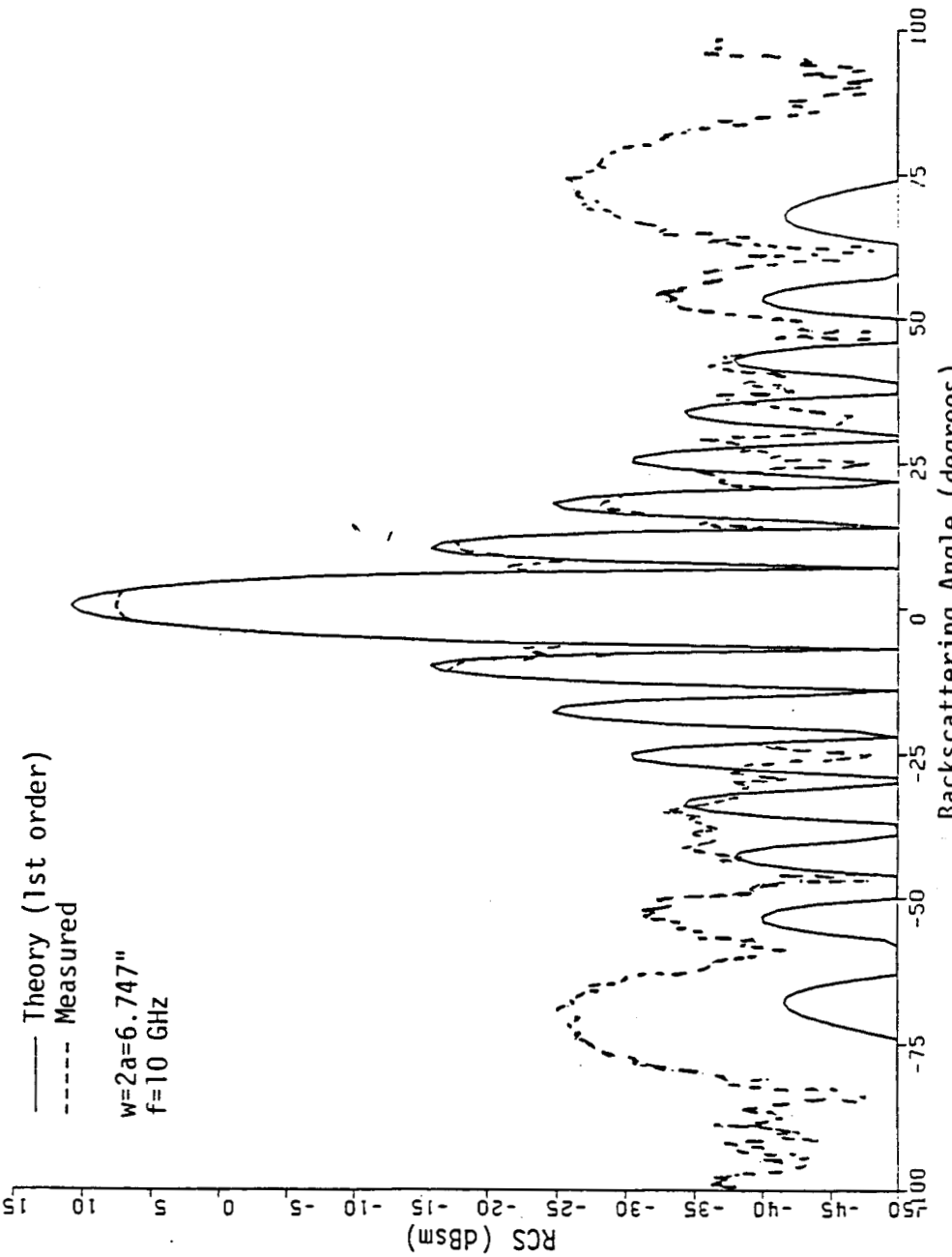

Figure 21. Primary VV polarization measured and predicted monostatic RCS patterns of a square plate in the off-principal plane $\phi = 45°$.

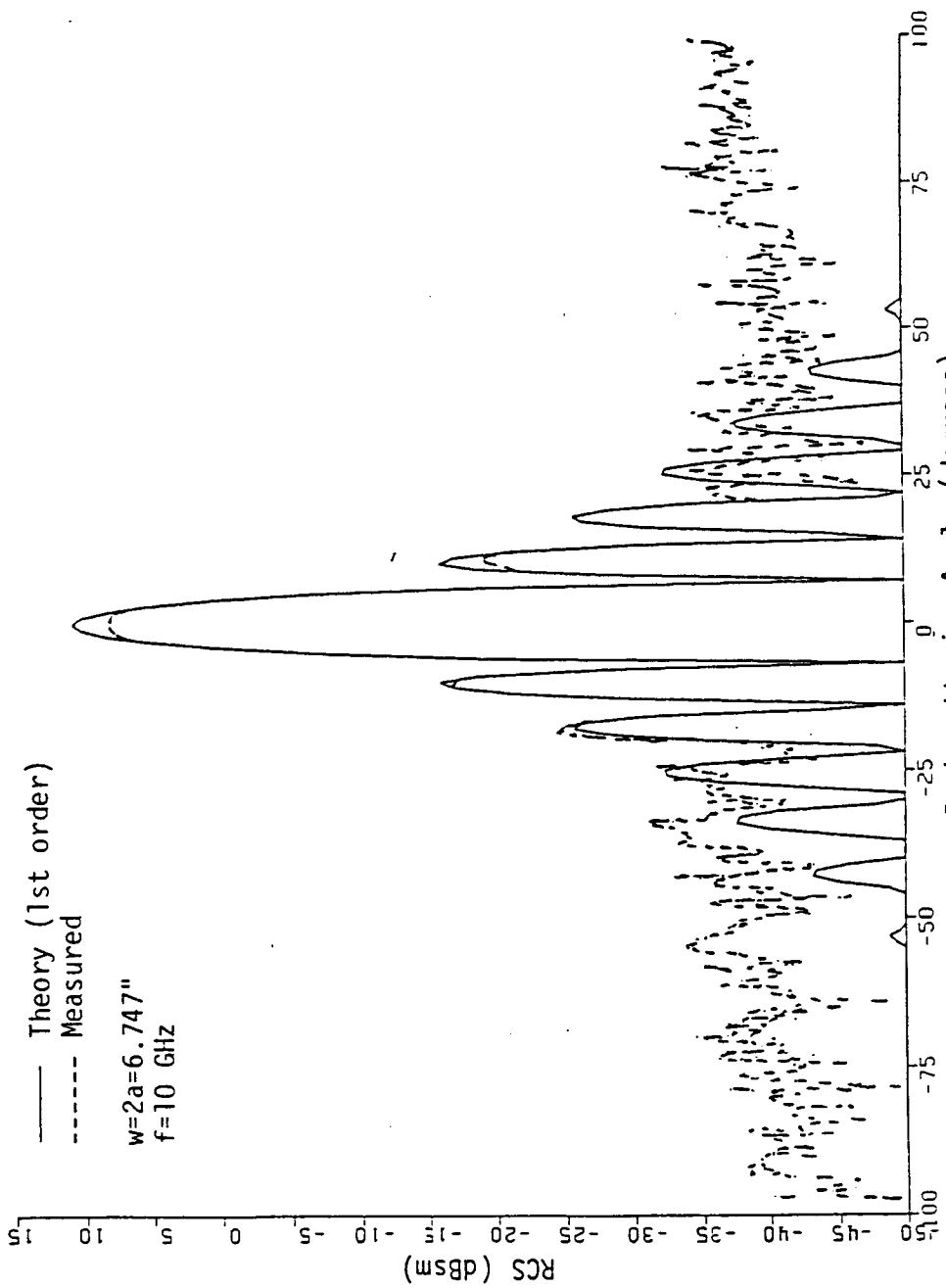

Figure 22. Primary HH polarization measured and predicted monostatic RCS patterns of a square plate in the off-principal plane $\phi = 45°$.

IV. REFERENCES

[1] R. G. Kouyoumjian and P. H. Pathak, "A uniform geometrical theory of diffraction for an edge in a perfectly conducting surface," *Proc. IEEE*, vol. 62, no. 11, pp. 1448-1461, Nov. 1974.

[2] J. L. Volakis, "A uniform geometrical theory of diffraction for an imperfectly conducting half-plane," *IEEE Trans. Ant. Prop.*, vol. AP-34, no. 2, pp. 172-180, Feb. 1986.

[3] J. L. Volakis, "Simple expressions for a function occuring in diffraction theory," *IEEE Trans. Ant. Prop.*, vol. AP-33, no. 6, pp. 678-680, June 1985.

[4] T. B. A. Senior, "Impedance boundary conditions for imperfectly conducting surfaces," *Appl. Sci. Res.*, sec. B, vol. 8, nos. 5-6, pp. 418-436, 1960.

[5] W. D. Burnside, "Analysis of on-aircraft antenna patterns," Ph.D. dissertation, Ohio State University, 1972.

[6] R. Tiberio, F. Bessi, G. Manara, and G. Pelosi, "Scattering by a strip with two face impedances at edge-on incidence," *Radio Science*, vol. 17, no. 5, pp. 1199-1210, Sept.-Oct. 1982.

[7] T. B. A. Senior, "Disk scattering at edge-on incidence," *IEEE Trans. Antennas Propagat.*, vol. AP-17, no. 6, pp. 751-756, Nov. 1969.

[8] C. E. Ryan, Jr. and L. Peters, Jr., "A creeping wave analysis of the edge-on echo area of disks," *IEEE Trans. Antennas Propagat.* (Communications), vol. AP-16, pp. 274-275, March 1968.

[9] R. DeVore, D. B. Hodge, R. G. Kouyoumjian, "Backscattering cross sections of circular disks for arbitrary incidence," *J. Appl. Phys.*, vol. 42, no. 6, pp. 3075-3083, July 1971.

[10] M. E. Bechtel, "Application of geometric diffraction theory of scattering cones and disks," *Proc. IEEE*, vol. 53, pp. 877-882, August 1965.

[11] E. F. Knott, T. B. A. Senior, P. L. E. Uslenghi, "High frequency backscattering from a metallic disc," *Proc. IEEE*, vol. 118, no. 12, pp. 1736-1742, December 1971.

[12] R. G. Kouyoumjian, "The geometrical theory of diffraction and its application," Chapter 6 in *Numerical and Asymptotic Techniques in Electromagnetics (R. Mittra, ed.)*, New-York: Springer-Verlag, 1975.

[13] A. Michaeli, "Equivalent edge currents for arbitrary aspects of observation," *IEEE Trans. Antennas Propagat.*, vol. AP-32, no. 3, March 1984.

[14] A. Michaeli, "Elimination of infinities in equivalent edge currents, part I: Fringe current components," *IEEE Trans. Antennas Propagat.*, vol. AP-34, no. 7, pp. 912-918, July 1986.

[15] A. Michaeli, "Elimination of infinities in equivalent edge currents, part II: Physical optics components," *IEEE Trans. Antennas Propagat.*, vol. AP-34, no. 8, pp. 1034-1037, August 1986.